# Chaotic Advection Mixer for Capturing Transient States of Diverse Biological Macromolecular Systems with Time-Resolved Small Angle X-ray Scattering

Authors Kara A. Zielinski<sup>1</sup>, Andrea M. Katz<sup>1</sup>, George D. Calvey<sup>1</sup>, Suzette A. Pabit<sup>1</sup>, Shawn K. Milano<sup>2</sup>, Cody Aplin<sup>2</sup>, Josue San Emeterio<sup>1</sup>, Richard A. Cerione<sup>2,3</sup>, and Lois Pollack<sup>1</sup>

- 1. School of Applied and Engineering Physics, Cornell University, Ithaca, NY, USA
- 2. Department of Chemistry and Chemical Biology, Cornell University, Ithaca, NY, USA
- 3. Department of Molecular Medicine, Cornell University, Ithaca, NY, USA

**Synopsis** A chaotic advection mixer expands the range of the types of reactions that can be probed with time-resoled solution scattering.

**Abstract** in time-resolved structural techniques, mainly in macromolecular crystallography and Small Angle X-ray Scattering (SAXS), allow for a detailed view of the dynamics of biological macromolecules and reactions between binding partners. Of particular promise, are mixand-inject techniques, which offer a wide range of experimental possibility as microfluidic mixers are used to rapidly combine two species just prior to data collection. Most mix-and-inject approaches rely on diffusive mixers, which have been effectively used with crystallography and SAXS for a variety of systems, but their success depends on a specific set of conditions to facilitate fast diffusion for mixing. The use of a new chaotic advection mixer designed for microfluidic applications helps to further broaden the types of systems for compatibility with time-resolved mixing experiments. The chaotic advection mixer can create ultra-thin, alternating layers of liquid, enabling faster diffusion so that even more slowly diffusing molecules, like proteins or nucleic acids, can achieve fast mixing on timescales relevant to biological reactions. This mixer was first used with UV-Vis absorbance and SAXS experiments with systems of a variety of molecular weights, and thus diffusion speeds. Careful effort was also dedicated to making a loop-loading sample delivery system that consumes as little sample as possible, enabling the study of precious, lab purified samples. The combination of the versatile mixer with low sample consumption opens the door to many new applications for mix-and-inject studies.

Keywords: Mixing; SAXS; Time-Resolved

#### 1. Introductions

Biological macromolecules are dynamic molecular machines that perform functions essential to life. Much insight into their function has been gained from probing their structures, dynamics, and interactions with binding partners. Time-resolved techniques for measuring structures are a powerful tool for observing molecular interactions, providing insight into both the underlying principles and the development of therapeutics to modify these interactions. Reactions must be rapidly initiated, and subsequently probed as they progress, at different timepoints. Many structural probes have been employed to capture transiently existing structures. These include crystallography (Moffat, 1998;

Olmos *et al.*, 2018; Pandey *et al.*, 2021), spectroscopies (van Nuland *et al.*, 1998; Calvey *et al.*, 2020), Small Angle X-ray Scattering (SAXS) (Plaxco & Dobson, 1996; Pollack *et al.*, 1999; Plumridge *et al.*, 2018), and cryo-electron microscopy (Lu *et al.*, 2009; Frank, 2017).

SAXS is particularly well suited for time-resolved studies, reporting the overall size, shape and degree of compactness of dynamic ensembles of molecules in solution at room-temperature (Svergun & Koch, 2003). Its solution nature provides a distinct advantage over other methods which require constraints, such as crystallization, labeling, the presence of spectroscopically active species, or freezing. SAXS probes molecules ranging in size from a few kDa to GDa (Kikhney & Svergun, 2015), is sensitive to intermolecular interactions and molecular weight, and can provide structural information on the 10s of Angstrom scale. Other light scattering techniques, like Dynamic Light Scattering (DLS), can provide similar information, but at much lower resolution. In addition, timeresolved SAXS (TR-SAXS) can detect the structures of transient interactions that seed the formation of larger complexes. At the concentrations required for many structural studies, samples may form higher order assemblies in equilibrium, and in some cases, this process is biologically relevant and can more closely mimic cellular environments. The ability to monitor the earliest structural intermediates (for example those resulting from bi-molecular interactions that precede large scale association), provides unique information about how complexes form. These first steps can offer novel insight into how large structures assemble, and can be directed at either ordered structures such as viruses (Khaykelson & Raviv, 2020), or disordered structures that arise, e.g. from liquid-liquid phase separation (Martin et al., 2021).

The two broad categories of TR-SAXS experiments are distinguished by the reaction trigger used: light-activated or chemically-triggered processes. Light can trigger photoisomerization, a temperaturejump, or the release of a caged compound (Cho et al., 2021; Thompson et al., 2019; Monteiro et al., 2021). However, most biological macromolecules are not light-activated, limiting the reach of this trigger. Chemically-triggered processes, enabled by rapid mixing of solutions, can be applied to a broader range of systems. Previous SAXS mixing experiments utilized stopped, continuous, or turbulent flow mixers (Pollack & Doniach, 2009; Graceffa et al., 2013). In a stopped-flow experiment, two solutions are rapidly mixed and injected into an observation chamber. The flow is stopped, trapping the reacting sample in the observation chamber. Measurements of the stationary sample occur as the mixture ages, in real time. To reach the shortest points, rapid exposure is required, resulting in noisy data, and the need to repeat the experiment many times to accumulate good statistics. Stopped-flow mixers are sample-intensive, using hundreds of microliters of sample per shot (Panine et al., 2006). Radiation damage may occur when measuring longer time points, forcing an attenuation of the X-ray beam. In continuous flow mixing, two solutions are rapidly mixed, then travel down an observation channel to allow the reaction to progress for a set amount of time before encountering the X-ray beam. Many of these mixers exploit diffusion via flow-focusing, which

utilizes a second co-flowing fluid stream to thin the central, sample-containing stream. Small molecules contained in the sheath rapidly diffuse into the sample stream, initiating the reaction. These mixers consume far less sample than stopped flow, but the thin ribbon of sample requires a small Xray beam and longer acquisition times to acquire high signal-to-noise data (Pollack et al., 2001; Lamb et al., 2008) unless an expanded observation region is present (Plumridge et al., 2018). For optimal performance, the reactant molecule should be small (e.g., quickly-diffusing) and highly soluble. These constraints preclude study of some small molecule drug targets, which are typically hydrophobic, have low solubility, or are unavailable in large quantities. It can also be difficult, with a diffusive mixer, to achieve one-to-one mixing ratios or to probe concentration sensitive reactions; the concentration of the diffusing reactant increases along the detection channel. Rapid reactions between macromolecular species (e.g. protein-protein or protein-nucleic acid interactions), or in viscous media, can be limited by slower diffusion times. Under some circumstances, mixing times could exceed the timescales of interest for the reaction (~ milliseconds to single seconds). Turbulent mixers circumvent some of the above challenges. They eliminate the need for a thin sample stream, produce higher signal-to-noise data in shorter collection time, and allow study of a broader range of reactions. Their drawback is the high sample consumption as very high sample flow rates are required to mix efficiently. Instrumentation advances significantly reduced the sample consumed by a turbulent SAXS mixer to 2-3 mg per time point (Graceffa et al., 2013), but this quantity may still be prohibitive for some biological samples.

A chaotic advection mixer, also known as a static mixer, bypasses all the above-described limitations. These mixers consist of a fluidic channel containing carefully arranged geometric elements that induce mixing via a process known as a baker's transformation (Figure 1). As two fluids travel down the channel, the elements stretch the interfaces between the fluids, split them apart, and then stack them to create thinner layers with more interfaces (Saatdjian et al., 2012; Wiggins & Ottino, 2004). Several baker's transformations occur as the fluids traverse the static mixer, so that many alternating thin "strips" of each fluid are formed. Static mixers are used in industry, and some designs can be scaled down and incorporated into microfluidic channels for efficient, laminar flow mixing of small volumes (Knoška et al., 2020; Bertsch et al., 2001). The production of thin layers of fluid via the baker's transformation are the key to extremely efficient mixing as even large macromolecules, or those in viscous media, can diffuse rapidly to mix across these very small length scales. These shorter length scales also yield tighter reaction initiation, and complete mixing. Because concentration sensitive reactions require a fixed ratio of reactant to sample, they can be readily performed in this platform. The chaotic advection mixer uses significantly less sample than a turbulent mixer, and its continuous flow nature greatly reduces SAXS radiation damage relative to a stopped flow mixer, making it an extremely unique and versatile option for performing time-resolved measurements.

Here, we present a novel application of a chaotic advection mixer with a custom sample environment that further reduces sample consumption. This system is optimized for efficient and effective acquisition of TR-SAXS data and includes a high throughput loop loading sample delivery system. Using a scaled-down version of an industrial static mixer, a Kenics design, this device produces high signal-to-noise data using only 1/10 of the sample required per timepoint by the most efficient turbulent SAXS mixer (Graceffa *et al.*, 2013), yet retains the ability to study a diverse range of biological interactions, regardless of biomacromolecule size, solubility, or viscosity. We describe the mixer design, construction, use, and highlight applications to a broad range of biological systems to show its efficacy in probing protein-protein associations (trypsin and aprotinin), protein-nucleic acid binding (GAC rRNA and L11 protein), Mg-induced RNA folding, concentration sensitive reactions, and the ability to observe molecules pre-aggregation (tissue transglutaminase with calcium), demonstrating all the applications introduced above.

#### 2. Materials and methods

### 2.1. Sample Preparation

Horse heart myoglobin was purchased from Sigma-Aldrich (M1882, T8003, A1153, St. Louis, MO) and was dissolved in 100 mM sodium phosphate, pH 7.8, filtered to remove aggregates and impurities, and adjusted to a concentration of 1.5 mM. A stock solution of 1% sodium azide (786-750, G-Biosciences, St. Louis, MO) was diluted with distilled water to produce concentrations ranging from 15-50 mM sodium azide.

Trypsin from bovine pancreas and aprotinin from bovine lung were purchased as lyophilized powders (T1426 and A1153, Sigma-Aldrich, St. Louis, MO) and were separately dissolved in 20 mM TRIS buffer, pH 7.0 with 40 mM KCl and 20 mM CaCl<sub>2</sub>. Protein concentrations were assessed from absorption measurements at 280 nm using extinction coefficients of 36,600 (M-cm)<sup>-1</sup> for trypsin and 3,840 (M-cm)<sup>-1</sup> for aprotinin. For mixing experiments, aprotinin at 270 mM (1.73 mg/mL) was chosen to be in molar excess of trypsin. The trypsin concentration of 170 mM (4 mg/mL) was chosen for these experiments as a compromise between signal strength and avoiding interparticle interference effects.

The 58-nucleotide GAC ribosomal RNA from E. coli with the U1061A mutation (Grilley *et al.*, 2007) was transcribed from PCR-amplified DNA plasmid using T7 polymerase kit (PROMEGA, Madison, WI). The RNA was purified from the T7 product using a Superdex 200 Increase 10x300 Size Exclusion Column (GE Healthcare, Chicago, IL) in 100 mM KCl and 10 mM Na-MOPSO buffer, pH 6.5. The RNA was concentrated in the same buffer and annealed at 65°C for 30 minutes, slowly cooled to room temperature and stored at 4°C prior to SAXS measurements. RNA concentration was determined from absorption measurements at 260 nm, using extinction coefficient 594,200 (M-cm)<sup>-1</sup>. For folding experiments, 60-80 mM RNA was mixed with 10 mM MgCl<sub>2</sub> in the same buffer. For

binding experiments, 60-80 mM RNA was mixed with 80-100 mM of L11 protein with 10 mM MgCl<sub>2</sub> in the same buffer.

The 147-residue full-length L11 ribosomal protein from T. thermophilus was purified as described previously (Triantafillidou *et al.*, 1999). In brief, BL21(DE3) *E. coli* cells were transformed with Histagged L11 recombinant plasmid with a thrombin cleavage site (pD431-SR/TthL11, made by DNA 2.0, Newark, CA). The cells were grown at 37°C until an optical density (OD) of 0.6 was reached. The expression of L11 protein was induced by the addition of 1 mM IPTG to the growth medium. To harvest the protein, the cells were centrifuged 4 hours after induction and the pellets were collected, reconstituted, and lysed using an Emulsiflex cell disruptor. The resulting crude lysate was passed through a Co<sup>2+</sup> column (HiTrap Talon crude, GE Healthcare, Chicago, IL) and the Histidine-tag was cleaved using a thrombin cleavage kit (Thrombin CleanCleave Kit, Sigma-Aldrich, St. Louis, MO). The efficiency of the cleavage and the purity of the protein was assessed using an SDS-PAGE. L11 protein was buffer exchanged into 100 mM KCl, 10 mM Na-MOPSO buffer, pH 6.5, prior to SAXS measurements. Protein concentration was determined from absorbance at 280 nm, using the extinction coefficient of 8,480 1/(M-cm).

Recombinant tissue transglutaminase (tG) was expressed and purified as previously described (Datta et al., 2006). Briefly, E. coli BL21 (DE3) competent cells (New England Biolabs) were transformed with a pET28a vector encoding human tG with a N-terminal six-histidine tag. The E. coli cells were grown in Luria broth (LB) with 50 µg/mL kanamycin at 37°C to an OD<sub>600</sub> of 0.6-0.8, and protein expression was induced at 25°C with 10 µM IPTG for 16-18 hours. The cells were resuspended in lysis buffer (50 mM Tris pH 8.5, 500 mM NaCl, 0.1 mM PMSF, 5 mM β-mercaptoethanol (BME), 10 % (weight/volume) glycerol, 50 μM GTP) and disrupted by sonication. The lysate was clarified by centrifugation at  $185,000 \times g$  for 45 minutes. The supernatant was then loaded onto a 5 mL HisTrap HP column (Cytiva Life Sciences) equilibrated with equilibration buffer (50 mM Tris pH 8.5, 500 mM NaCl, 10 % (weight/volume) glycerol, 0.1 mM PMSF, 5 mM BME), washed with 100 mL of equilibration buffer, and then washed again with 100 mL of wash buffer (50 mM Tris pH 8.5, 10 mM NaCl, 10 % (weight/volume) glycerol, 5 mM BME). The protein was isocratically eluted with 50 mL of wash buffer with 320 mM imidazole. The eluent was loaded onto a 5 mL HiTrap Q HP column (Cytiva Life Sciences) and eluted with a gradient of Buffer A (50 mM MES pH 6.5, 10 mM NaCl, 10% (weight/volume) glycerol, 1 mM DTT) and Buffer B (Buffer A with 800 mM NaCl). The peak fractions were then pooled and loaded again onto a 5 mL HisTrap column equilibrated with HisTrap Buffer A (20 mM HEPES pH 7.5, 100 mM NaCl, 10 % (weight/volume) glycerol), washed with 100 mL of HisTrap Buffer A, then eluted over a gradient with HisTrap Buffer B (HisTrap Buffer A with 500 mM imidazole). The peak fraction was then pooled and injected onto a HiLoad Superdex 200 column (Cytiva Life Sciences) equilibrated with tG gel filtration buffer (20 mM HEPES pH 7.5, 100 mM NaCl, 10% (weight/volume) glycerol, 1 mM DTT) for purification by size-exclusion

chromatography. The purified tG was concentrated to 2 mg/mL using a 10 kDa cutoff centrifugal filter (Jumbosep, PALL), flash froze in liquid nitrogen, and stored at -80°C. For time-resolved experiments, 2 mg/mL tG was mixed with 4 mM CaCl<sub>2</sub> in the same gel filtration buffer.

#### 2.2. Time-Resolved Absorbance Measurements for Kenics Mixer Characterization

Time-resolved absorbance experiments were performed to verify mixing using  $560 \pm 2$  nm light and a Zyla CMOS camera (ANDOR, Oxford Instruments, Abingdon, UK) to illuminate and image the sample cell. The microscope was configured so that the field of view of the camera is several mm, therefore one image captured the reaction across a range of timepoints. Calibrations were performed using a well characterized reaction: myoglobin plus sodium azide (Marcoline & Elgren, 1998; Nami et al., 2016).

PHD 4400 syringe pumps (Harvard Apparatus, Holliston, MA) were used to drive reacting solutions into the supply lines at 55.5  $\mu$ L/min each. The sheath solution, driven at 189  $\mu$ L/min by an OB1 pressure controller with feedback from an MFS flow sensor (Elveflow, Paris, France), contained sodium azide at the final mixed concentration to maintain a constant sodium azide concentration in the sample cell. These flow rates were chosen so that the camera could image a 10-90 ms reaction interval with a mixed sample pathlength of 250  $\mu$ m. The reaction was probed at three sodium azide concentrations: 15 mM, 20 mM, and 25 mM, with both Kenics mixer designs. Data were also acquired when mixing with water for use as a reference. Dark counts were subtracted from all images. For each dataset, the transmission at each pixel was calculated as a ratio of the reacted data over the reference data, and then converted to absorbance. Flow velocities were used to convert the distance from the Kenics mixer to a timepoint. This yielded the final dataset of absorbance vs time that was used for kinetics modelling.

## 2.3. SAXS Experiments

## 2.3.1. Beamline Requirements

All samples were characterized by static, equilibrium SAXS to find optimal conditions. GAC rRNA, L11, trypsin, and aprotinin were screened at CHESS beamline ID7A1. For tG, SAXS conditions were screened using a home source (BioXolver, Xenocs Inc., Holyoke, MA). Time-resolved SAXS experiments were performed at CHESS beamline ID7A1. X-ray energies of 11.3 keV were used. Beam size was maintained at 120 by 150 µm by using custom made single crystal Ge slits inspired by Li *et al.*, 2008. Normalization of scattered intensities was achieved using a semi-transparent beam stop made of 250 micron thick molybdenum foil, which can block the direct beam to prevent detector damage while still providing a measure of transmitted counts for normalization (Kučerka *et al.*, 2008).

## 2.3.2. Sample Delivery Setup

The sample delivery system must efficiently deliver all reactants to the mixer, allow easy switching between biomolecules and buffers for background subtraction with minimal dead volume, and fast flowrate stabilization to conserve sample. These criteria are met with a loop loading system, in which each species, sample or buffer, is loaded into two sets of separate loops (four loops total), connected to each of the two sides of the mixer. The loop volume was 75  $\mu$ L for the sample and 150  $\mu$ L for the buffer. Two high pressure syringe pumps (PHD 4400, Harvard Apparatus, Holliston, MA) were used to drive syringes of inert mineral oil to push the species out of the loops and into the mixer. Two sets (one for each inlet port of the Kenics) of three valves (two high pressure switching valves (Rheodyne MXP7970, IDEX Health and Science, West Henrietta, NY) and one injection valve (VICI Valco Instruments Co. Inc., Houston, TX)) were used to control this process (see SI for more details and benefits). This setup also prevented the oil from entering the sample cell. Another injection valve (Rheodyne MXP7970, IDEX Health and Science, West Henrietta, NY) was used for automatic oil refilling of the syringes. An automatic cleaning station, with soap and water reservoirs pressurized with nitrogen gas, was used to remove the oil, clean, and dry the loops so that they were ready for the next sample. To increase efficiency, the sample collection and cleaning was automated through custom software that remotely controlled all pumps and valves. The supply lines connected directly to the mixer had inner diameters of 75-100 micron to reduce dead volumes and to keep the back pressure compatible with the range of the syringe pumps. More details of our sample delivery setup can be found in the SI (Figure S1).

A sheath flow, which surrounds the mixed sample, was driven by a multichannel pressure controller (OB1, 0-8000 mbar range, Elveflow, Paris, France), and measured with flow sensors (MFS3 or MFS4 depending on flow conditions, Elveflow, Paris, France). The flow through the waste line of the device was monitored by a mass flow sensor (ML120V00 Mini Cori-flow, Bronkhorst USA Inc, Bethlehem, PA) which, in combination with the upstream MFS flow sensor, was used to monitor the total flow rate through the sample cell and to ensure that the correct conditions were met while acquiring data. A schematic of the flow set up and operation protocols are provided in SI (Figure S1).

#### 2.3.3. Data Analysis

Scattering images from samples and from buffer (without samples) were collected and analyzed using BioXTAS RAW software (Nielsen *et al.*, 2009). For each measurement, datasets were comprised of 10-20 5 second frames. To extract the signal from the biomolecules alone, SAXS measurements from the buffer alone were subtracted from the SAXS profiles that contained the molecular sample(s). Guinier fits were used to calculate radius of gyration (R<sub>g</sub>) values, except for the trypsin and aprotinin series, which utilized P(r) instead due to small amounts of aggregation present in both samples before the reaction. Further data processing was performed using in-house MATLAB scripts.

#### 3. Results

## 3.1. Chaotic Advection Mixer Concept, Design, Fabrication, Operation and Testing

## 3.1.1. Mixer Concept

As described in the introduction, our goal is to optimize a static mixer for TR-SAXS experiments. One of the more easily adaptable static mixers is based on the Kenics design (Chemineer, Dayton, Ohio), shown in Figure 1B. Short, helical elements with alternating left- or right-handedness induce baker's transformations (Figure 1A) as the flow passes through them (Bertsch *et al.*, 2001; Galaktionov *et al.*, 2003; Hobbs & Muzzio, 1997). The aspect ratio, twist angle, and number of helices can be optimized to mix the fluids of interest (Galaktionov *et al.*, 2003; Szalai & Muzzio, 2003), we selected a twist angle of 135° and an aspect ratio of 1.125 based on our simulations (ANSYS Fluent 18.2, ANSYS, Inc., Canonsburg, Pennsylvania). After passage through the Kenics element, the solution flows along a tube, where the distance travelled corresponds to the time point measured. Figure 1A shows a simulation of the baker's transformation at various points throughout the first five helical elements, showing the expected 2<sup>n+1</sup> layers after n blades with the "strip" pattern that agrees with simulations in the literature.

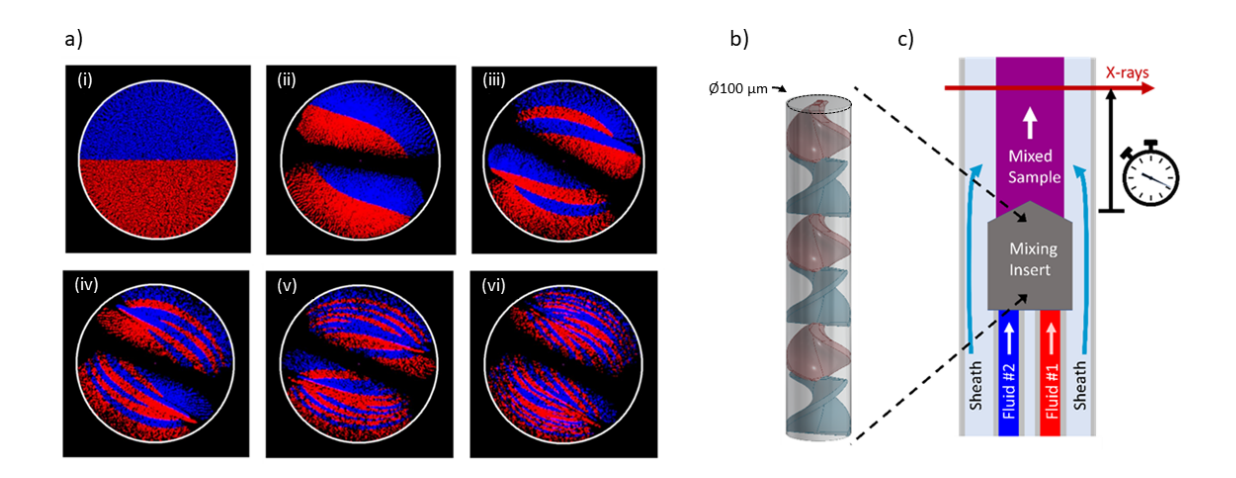


**Figure 1** Simulation (ANSYS Fluent 18.2, ANSYS, Inc., Canonsburg, Pennsylvania) and conceptional design of the Kenics mixer. (a) Cross sectional view of the simulated flows at different locations inside a Kenics mixer with twist angle of 135° and aspect ratio of 1.125. Locations are as follows: (i) immediately before the flows encounter the first element, (ii) after one helical element, (iii) after two elements, (iv) after three elements, (v) after four elements, (vi) after five elements. These images have been smoothed to increase the apparent size of the streamlines to make them easier to see. This may reduce or eliminate the visibility of thinner striations in the later panels. (b) Kenics mixer. The cylindrical pipe through which liquid flows is drawn in transparent gray. (c) Overall device concept. A mixing insert (gray) combines two fluids (red and blue). The mixed sample

(purple) flows out of the insert and is surrounded by a sheath flow (light blue). X-rays probe the mixed sample after a pre-determined delay.

There are several important considerations when interfacing this design with X-rays. First, once the solution emerges from the mixing region, it should be fully sheathed in (surrounded by) water or buffer to keep the sample off the walls of the observation channel (Figure 1C). This is important because sample flowing near the walls is susceptible to radiation damage (Kirby *et al.*, 2016). Constraining the sample to the center of the channel also reduces timing dispersion resulting from the parabolic flow profile. If a small ligand or ion is being mixed and has a large enough diffusion coefficient (on the order of 10<sup>-9</sup> m²/s) to diffuse appreciably in the radial direction of the sample cell, the concentration of the ligand can be kept constant in the sample cell by including the ligand in the sheath flow. Second, the cross section of the mixed fluid in the X-ray observation region should be large enough to accommodate the X-ray beam and to generate a strong scattering signal. Third, the tube that comprises the observation region should be made from X-ray transparent material with low intrinsic scatter. Finally, the diameter of the observation region should be such that a good compromise is made between X-ray signal strength (larger diameter) and reasonable timing uncertainty due to sample transit times through the beam (smaller diameter). Figure 1C shows a conceptual drawing of a device that has all these desired qualities.

#### 3.1.2. Mixer Design

Mixing inserts, which house the helical elements of the Kenics and include ports for the capillaries, were designed in Autodesk Inventor 2016 and fabricated using a commercial 3D direct laser writing setup (Photonic Professional GT, Nanoscribe GmbH, Stutensee, Germany; Niesler & Hermatschweiler, 2014; Maruo *et al.*, 1997). Two insert designs, with either a cone opening tip or a straight opening tip, were used (Figure 2, Figure S2). The exterior of the cone opening design is shown as a CAD rendering in Figure 2A. The tip of the insert in this design has a cone shape with a 250  $\mu$ m diameter and contains a cross-shaped homogenizer so that the mixed flow emerges at its fully expanded diameter (Figure 2B). This design is ideal for capturing fast reaction timepoints, e.g., immediately after mixing, which requires acquiring data a short distance from the tip. Figure S2A shows the exterior of the second, straight opening design, which has a tip that is 150  $\mu$ m in diameter (Figure S2B). When the mixed sample exits this insert, it needs to expand to its final width of 250  $\mu$ m. More information about the second design can be found in the SI.

For both designs, fins center the insert in the observation tube while allowing the sheath to flow around it, as shown in the orthographic view in Figures 2A. The supply line ports each accommodate a 200 µm outer diameter fused silica capillary (Polymicro Technologies, Phoenix, AZ), which can be glued in place with UV curable epoxy (Master Bond Inc., Hackensack, NJ). Constricted regions center the supply lines in the ports. For the cone opening design, fluids leaving each supply line are

combined in a  $\sim$ 1 mm long, 100  $\mu$ m diameter channel containing the Kenics mixing elements and then exit through the cone shaped ending (Figure 2E). Eight helical mixing elements are present in the cone opening design. Given our simulation results, 8 elements in a 100  $\mu$ m channel produce  $\sim$ 200 nm thick layers of fluid. For a typical protein (diffusion coefficient  $\sim$ 10<sup>-11</sup> m²/s; Young *et al.*, 1980) nearly complete mixing is achieved within several milliseconds. The insert can be modified for different mixing efficiencies if desired.

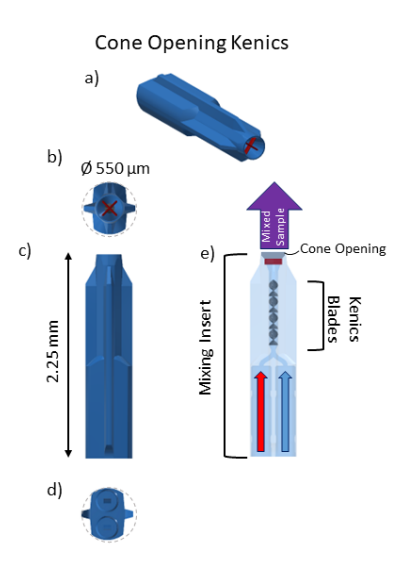


**Figure 2** CAD rendering of the 3D printed mixing insert that houses the Kenics mixer. a) Exterior of the device. b) View of the cone opening from downstream, with flow homogenizer shown in red. The dashed grey line represents the observation tube. c) Side view of the cone opening insert. d) View of the cone opening insert from upstream, showing the supply line ports. e) Cross-sectional view of the cone opening insert with the cone opening shaded in grey.

## 3.1.3. Mixing Insert and Sample Cell Fabrication

Mixing inserts were 3D printed and completed inserts were stored in the developer until needed. Inserts were rinsed with isopropanol to remove developer and allowed to dry fully before assembly (Knoška *et al.*, 2020). More details of device fabrication are provided in the Supporting Information and Figures S3-S4. Briefly, the process entails bonding two supply lines to the mixer, surface treating the mixer to make it less hydrophobic (Sobiesierski *et al.*, 2015; Wang *et al.*, 2005), and then using custom sample cell holders to place the mixer inside thin-walled X-ray compatible glass tubing (Hilgenberg GmbH, Malsfeld, Germany) to complete the device.

## 3.1.4. Mixing Times and Computing Final Timepoint Probed

Mixing is considered complete when the concentration of the reacting species is 1:1 in the mixer; every molecule theoretically has access to a binding partner. In both designs, the mixing occurs as the two solutions traverse the insert, but the point at which full mixing is achieved depends on the size

and diffusion coefficient of the molecules being mixed and the viscosity and densities of the buffers. For example, mixing a macromolecule (protein or nucleic acid) with a small additive (ligand or ion) will be faster than mixing of two large macromolecules (two proteins or a protein and a nucleic acid). Therefore, we consider the relative size of the species being mixed to determine how many elements are required to fully initiate the reaction. This mixing time can be several ms or longer, depending on the flow rates. We use the following guiding principles to account for these differences: two large species are considered fully mixed after 8 helical elements; one large species and one intermediate ligand are fully mixed after 4 helical elements; and one large species and one small species are fully mixed after 1 helical element (Table 1). Of course, the molecules pass through all 8 elements, even if they are fully mixed after 4. This 8 element design provides maximum flexibility for the different types of reactions that can be probed, without hindering the ability to probe even the fastest timepoints ( $\sim$ 10 ms) for fast reactions. The total time spent in the mixer can be made small in most cases, but to account for some molecules reacting before all molecules in the sample are fully mixed, we approximate the uncertainty due to the travel time as half of the average transit time. Because most particles transit the mixer in about the same amount of time, this design presents a distinct advantage for time resolved studies where differences in travel time through the device (residence or transit time) can dramatically increase error bars on mixing times or time points (Galaktionov et al., 2003). A schematic of the different mixing initiation points is shown in Figure 3.

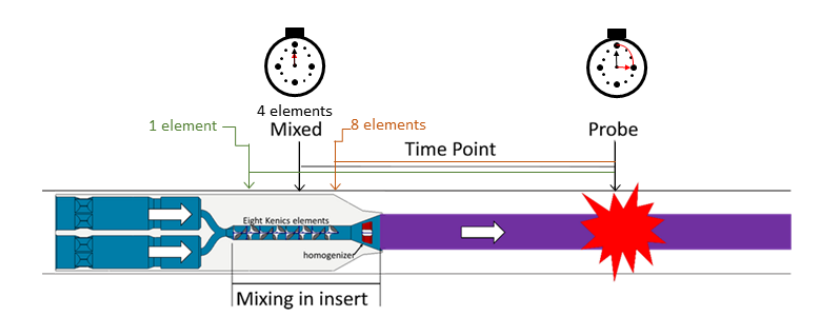


**Figure 3** Graphical depiction of mixing and the timepoint probed. The different mixed points are indicated. Note that the full 8 elements are always present, but the final mixing point occurs at different places depending on the systems probed.

**Table 1** Three Reaction Classes, based on the relative size of the species being mixed.

Reaction Classes	Species A	Species B	Number of Mixing Elements Needed for Full Mixing
	Protein	Protein	8 elements (full insert)
Two Large Species	Protein	DNA	8 elements (full insert)
	Protein	RNA	8 elements (full insert)
1 Large Biomacromolecule	Protein	Ligand	4 elements (half of insert)
+	DNA	Ligand	4 elements (half insert)
1 Intermediate Sized Ligand	RNA	Ligand	4 elements (half insert)
1 Large Biomacromolecule	Protein	Ion	1 element (eighth of insert)
+	DNA	Ion	1 element (eighth of insert)
1 Small Sized Ion	RNA	Ion	1 element (eighth of insert)

Once the fully mixed point has been determined, the flowrates and the distance from the tip of the insert dictate the final timepoint probed (schematically shown in Figure 3), based on an analytical solution of the Navier-Stokes and continuity equations. The details of the solutions and application of boundary conditions are reported in the supporting information. Briefly, a solution can be determined for flow velocities (u) of both sheath  $(u_{sh})$  and sample  $(u_s)$  as a function of the radial direction of the sample cell (r), where R is the radius of the sample cell and  $r_s$  is the radius of the inner sample stream), the pressure gradient along the z-axis (G=-dP/dz), the acceleration due to gravity (g), the viscosity of the fluids  $(\mu_{sh}, \mu_s)$ , and the density of the fluids  $(\rho_{sh}, \rho_s)$ .

For this work, all samples studied were water soluble and contained no additives that changed their viscosities or densities appreciably, thus we examine the case of  $\mu_{sh} = \mu_s = \mu_{water}$  and  $\rho_{sh} = \rho_s = \rho_{water}$ . In this regime, the simplified solutions are:

$$u_{sh}(r) = \frac{(G + \rho_{water}g)}{4\mu_{water}} (r^2 - R^2) \text{ for } r > r_s$$

$$u_s(r) = \frac{(G + \rho_{water}g)}{4\mu_{water}} (r^2 - R^2) \text{ for } r \le r_s$$

In addition to the time elapsed in the insert, uncertainties in the timepoint arise from the transit time of the sample through the area illuminated by the X-ray beam and from the parabolic flow profile of the sample traveling through the observation tube. These must be combined with the mixing time to find the total uncertainty in a measured timepoint. More details about these calculations and converting flow velocity to volumetric flowrate can be found in the SI.

For x-ray scattering experiments, a 250 µm diameter sample stream (surrounded by sheath) represents a good balance between sample consumption, timepoint dispersion, and path length (thickness of sample that is illuminated by the beam). Given the diameter of the outlet channel (550 µm), the chosen diameter of the sample stream determines the ratio of sample to sheath flow. With this ratio clearly defined, absolute flow speeds determine the accessible time regime. Access to shorter timepoints requires fast mixing and fast flow, both of which occur at higher sample flow rates, while access to longer time points can tolerate slower mixing and slower flow, with lower sample flow rates. With either Kenics design, time scales ranging from milliseconds to seconds can be easily accessed by varying the flow speeds of both components of the sample, and the sheath, and each timepoint can be reached by multiple combinations of flow speeds and distance from the tip. However, it is important to note that the flow speed affects mixing times and therefore the overall uncertainty associated with each time point. Selection of experimental conditions is a compromise between lower uncertainty (higher sample flow rate) and less sample consumption (lower flow rate).

The accessible timepoints span three orders of magnitude (~10-1000 ms) and can be changed by varying the flow conditions and position of the X-ray beam relative to the end of the insert. Table 2 provides a summary of the timepoints, uncertainties, and suggested x-ray locations attainable with each flow condition for Reaction Class 1 (two large macromolecules), using a cone opening device with a 250 µm X-ray sample pathlength in a 550 µm inner diameter sample cell. It also shows how different flow conditions can be used to reach the same timepoint, so that sample consumption and timing uncertainty can be balanced based on the needs and limitations for a specific system. A discussion of uncertainty calculations is in the SI. Additionally, the flow conditions for the other reaction classes and for the straight opening device (Tables S1-S4) and the reproducibility of the same timepoint with different flow conditions are also included in the SI (Figure S5).

**Table 2** Flow Conditions for Reaction Class 1: Two Large Biomacromolecules in the Cone Opening Device

Sample A Flow Rate	Sample B Flow Rate	Sheath Flow Rate	Timepoint	Distance from Tip
(μL/min)	(μL/min)	(μL/min)	(ms +/- uncertainty)	(μm)
60	60	203.1	10 +/- 6	293
60	60	203.1	20 +/- 6	705

30	30	101.5	20 +/- 12	292	
30	30	101.5	50 +/- 12	917	
30	30	101.5	100 +/- 13	1952	
20	20	67.7	100 +/- 18	1262	
20	20	67.7	250 +/- 23	3354	
10	10	33.8	250 +/- 38	1615	
10	10	33.8	500 +/- 46	3344	
10	10	33.8	1000 +/- 71	6793	

## 3.1.5. Mixer Characterization Using Visible Absorbance

Before mixers were used for TR-SAXS, control experiments were performed to assess their operation and efficacy. When azide binds to metmyoglobin, a change in absorbance occurs at several wavelengths in the UV-visible spectrum, including from about 550-575 nm(Marcoline & Elgren, 1998). This absorbance change can be easily captured in a custom-built long working distance microscope (described previously, Calvey *et al.*, 2016) so visible absorbance data on the myoglobin and azide system were acquired in a time-resolved experiment to characterize the effectiveness of both mixers, measure reaction kinetics, and determine the dead time of the mixers (Figure 4A-C).

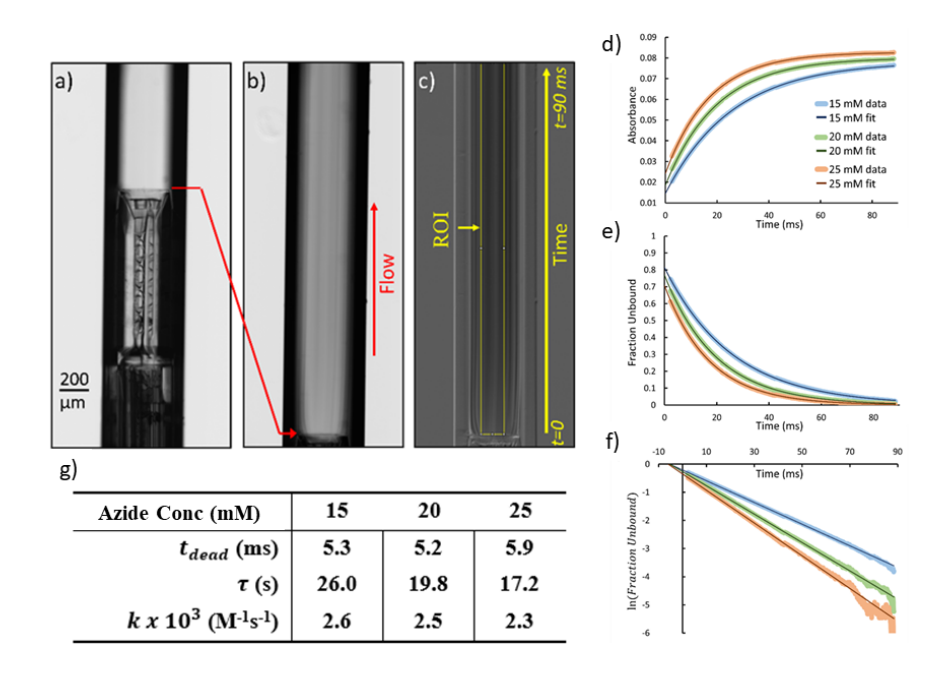


**Figure 4** Myoglobin and Azide Time-Resolved Absorbance Measurements in the cone opening device. Images of the cone opening Kenics and observation region during the absorbance experiment. a) Cone opening Kenics in the observation tube. b) Dark-subtracted image of the observation region for myoglobin mixing with azide. Striations visible in the image result from the cross-shaped homogenizer and occur in the reference image as well. c) Image showing transmission. d) Absorbance vs. time for each of the three azide concentrations, with fits overlaid. Legend applies to all panels. e) The fraction of unbound myoglobin vs. time. f) Log plot of fraction unbound vs. time. The slight discontinuity in the data at ~45 ms is due to a mismatch in the two modules of the camera's detector. g) Table showing the dead time ( $t_{dead}$ ), time constant ( $\tau$ ), and reaction constant (t) for each azide concentration. Notably, the k values are a good match to the literature ( $t_{dead}$ ). These values were extracted from fitting the absorbance vs. time data.

Figure 4D shows absorbance vs time for myoglobin reacting with different concentrations of azide in the cone opening Kenics. The data are well fit with a single exponential, as expected for the pseudo-first order chemical reaction, with the azide in vast excess:

$$A(t) = \Delta A(1 - e^{-\frac{t - t_{dead}}{\tau}})$$

Here  $\Delta A$  is the total change in absorbance,  $t_{dead}$  is the dead time (time between the beginning of the reaction and the point at which observations begin), and  $\tau$  is the time constant of the reaction. It should be noted that the dead time is context dependent; it varies according to the diffusion coefficients of the species being mixed, as well as the flow rates. The rate constant, k, can be determined according to:

$$\frac{1}{\tau} = C_{azide}k$$

Where  $C_{azide}$  is the azide concentration after mixing.

The absorbance data can be converted to report the fraction of unbound myoglobin over time (Figure 4E). As expected, higher azide concentrations result in faster decay in the unbound myoglobin fraction. In Figure 4F, the log of the fraction of unbound myoglobin is plotted. As expected from the pseudo-first order reaction, the data are well fit with a straight line. Here, the dead time is the time intercept, and  $-1/\tau$  is the slope.

The kinetics properties extracted from the fits are shown in Figure 4. The measured k values from this experiment agree well with a literature value of  $2.8 \pm 0.3 \times 10^3 \,\mathrm{M}^{-1}\mathrm{s}^{-1}$  for the same buffer conditions (Nami *et al.*, 2016), demonstrating that the insert mixes properly and that this device can be used to accurately measure reaction kinetics. Results from the straight-opening design and the derivation of

the formulas used to determine the rate constant and dead time are shown in the SI. Even with modest combined sample flow rates of 110 uL/min, the dead time is low enough to probe reaction timepoints below 10 ms, sufficient to capture side chain motions and allosteric transitions (Benkovic, 2003). Higher flow rates could be used to access shorter dead times in this device, if desired. Overall, these absorbance measurements show that this device is a robust tool for measuring chemical kinetics if proper sample preparation and filtering steps are taken.

### 3.2. Mixer Applications to TR-SAXS

To demonstrate the effectiveness of the Kenics mixer and its compatibility with SAXS, we used the different mixer designs to examine a broad range of reacting species. Reactions between molecules of different sizes were recorded, and different time ranges were accessed using the two different insert geometries. In this section, we report results on a variety of systems that highlight the versatility and breadth of the design. SASBDB accession codes for all data are provided in SI.

## 3.2.1. Comparing Diffusive and Chaotic Advection Mixing for Magnesium-driven GAC rRNA Folding

The first experiment examined Mg<sup>2+</sup> initiated RNA folding. RNA in buffered solutions containing monovalent salt possesses secondary but not tertiary structures. For many RNAs, Mg<sup>2+</sup> facilitates the formation of stabilizing, tertiary contacts (Draper, 2004). The system of interest is a 60 nucleotide GTPase center (GAC) ribosomal RNA (rRNA), whose folding was previously studied using a diffusive mixer (Welty et al., 2018). For these past experiments, GAC rRNA, in a monovalent salt solution flowed through a central channel and Mg<sup>2+</sup> was introduced via a coaxially flowing solution. The GAC rRNA was flow-focused into a thin stream to facilitate rapid mixing. We collected an initial state (no Mg<sup>2+</sup>), steady state (GAC rRNA incubated with Mg<sup>2+</sup> for several minutes), and five intermediate timepoints (10 ms, 30 ms, 50 ms, 100 ms, 300 ms, and 1000 ms) to track the progression of this RNA folding reaction (Figure 5A). Although structural changes were recorded over a broad range of scattering angles, as described in our previous publication, for the purposes of this study we focus on a single parameter, the RNA's overall size reported by its radius of gyration, Rg. Before the addition of  $Mg^{2+}$  to trigger folding, the RNA's  $R_g$  was 24 +/- 0.41 Å. Within 10 ms of the addition of Mg ions, the  $R_g$  decreases to 22.88 +/- 0.58 Å. Small changes in the  $R_g$  are observed as the reaction is followed to 1000 ms. By this time,  $R_g = 22.29 + -0.44 \text{ Å}$ , which agrees within error with the steady state value of 21.85 +/- 0.34 Å.

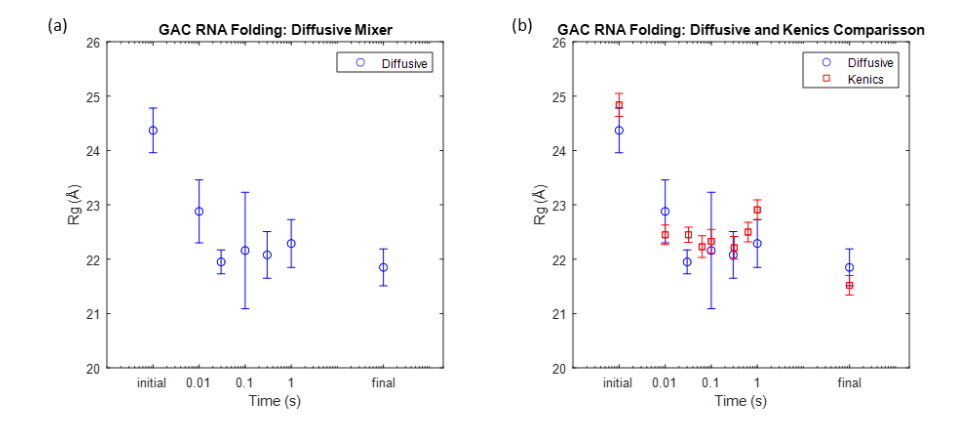


**Figure 5** GAC rRNA Folding Experiment. (a) The mean  $R_g$  of the RNA at different timepoints as the RNA is folding and becoming more compact as collected previously with the diffusive mixer (Welty *et al.*, 2018). (b) Comparing the folding of the RNA by looking at the  $R_g$  as a function of time with the diffusive mixer (blue) and Kenics device (red). The error bars are smaller for the Kenics data points because the reaction initiation is tighter so there is less of a spread in the age of the population.

We repeated this experiment with the Kenics mixer (cone opening device, Reaction Class 3) with GAC rRNA and Mg<sup>2+</sup> flowing through separate channels until they were rapidly combined inside the Kenics insert. We collected the initial, Mg-free state, a steady state point (GAC rRNA incubated with  $Mg^{2+}$ ), and seven intermediate timepoints (10 ms, 32 ms, 63 ms, 100 ms, 316 ms, 631 ms, and 1000 ms) to track reaction progress (Figure 5B). Good agreement is found when comparing the R<sub>g</sub> determined by the Kenics and diffusive mixers. In both cases, we observe a large, rapid compaction on the  $\sim 10$  ms time scale, which results in a transient state with comparable  $R_e$ . The ensuing fluctuations in R<sub>g</sub> through reaction times that reach 1000 ms are virtually identical between the two mixers. The R<sub>g</sub> measured at 1000 ms in the Kenics device is 22.91 +/- 0.18 Å, which is close to the R<sub>g</sub> measured in the diffusive mixer at 1000 ms (22.29 +/- 0.44 Å). This agreement demonstrates that the Kenics mixer accurately recapitulates prior TR-SAXS results for reactions of large and small species. Most notable is the reduction in uncertainty of R<sub>g</sub> in the Kenics mixers relative to its value obtained with the diffusive mixer. This sharpening likely results from the more efficient reaction initiation in the Kenics, and the reduced spread in reaction age, although other beamline and data collection improvements may also contribute. As shown in Figure 1, the baker's transformations, which initiate mixing inside the Kenics, create thin layers of liquid (200 nm), so the reaction initiation is almost uniform, especially for mixing with small, rapidly diffusing species such as Mg<sup>2+</sup>. This rapid and complete mixing stands in contrast with flow-focused mixing. In the former case, diffusion proceeds rapidly over a very short distance of ~200 nm, while the central focused jet of the diffusive mixer can be a few microns in diameter. Key to rapid, uniform mixing, is a minimization of the length scale for diffusion, which is only achieved by the Kenics.

## 3.2.2. Capturing Transient States of the Ca<sup>2+</sup>-driven Self-Association of tissue-Transglutaminase

A second application of the Kenics mixer that leverages the need to rapidly reach and maintain a fixed, final ligand concentration, is the study of some protein conformational changes. In the Kenics, mixing of the two species occurs quickly and uniformly. In contrast, in a diffusive mixer, the concentration of the small (diffusing) ligand steadily increases over time, which suffices for reactions which require a concentration threshold, but is not ideal for systems that are sensitive to the total ligand concentration. One system that benefits from the Kenics scheme is tissue-transglutaminase (tG) in the presence of Ca<sup>2+</sup>. tG is an enzyme that has a distinct 'open' and 'closed' state, which is modulated by the presence of Ca<sup>2+</sup> and GTP. Ca<sup>2+</sup> drives tG open and in this state, tG acts as a crosslinker. GTP closes tG, and in this state, tG acts as a GTPase (Liu *et al.*, 2002; Pinkas *et al.*, 2007). The increased expression of tG is linked to several different cancers (Mann *et al.*, 2006; Katt *et al.*, 2022). Interestingly, when tG is mutated to stay in an open conformation, it is toxic to cells (Datta *et al.*, 2007; Katt *et al.*, 2018) for reasons that are poorly understood. Thus, there is significant interest in studying this conformational change and exploring ways to stabilize the open state for therapeutic purposes.

We first studied the  $tG + Ca^{2+}$  reaction with static SAXS and found that the opening process was sensitive to both the concentration of  $Ca^{2+}$  and the reaction incubation time (Figure 6). When tG was incubated with  $Ca^{2+}$  for 5 minutes (fast-load), the final  $R_g$  is  $50.2 \pm 0.5$  Å, but when incubated for 30 minutes (slow-load), the  $R_g$  increases to  $68.6 \pm 1.3$  Å. This longer incubation time with  $Ca^{2+}$  results in more aggregation, as indicated by the increase in the SAXS intensity at zero angle, and the amount of aggregation seems to correlate with  $Ca^{2+}$  interaction time.

Due to the formation of higher order oligomers on the minute time scale, equilibrium SAXS cannot capture the first stages in the opening of tG. In contrast, TR-SAXS offers the opportunity to capture this transient state with the potential to capture the monomeric form and elucidate the mechanism of tG opening. We used the Kenics mixer (straight opening device (Figure S2), Reaction Class 3) to study this process. We captured an initial state (no Ca<sup>2+</sup>), a steady state (tG incubated with Ca<sup>2+</sup> for approximately 10 minutes), and six intermediate timepoints (32 ms, 63 ms, 100 ms, 316 ms, 631 ms, and 1500 ms; Figure 6).

We were surprised to find two relatively stable states with a sharp transition between 100 ms and 316 ms. We captured a transition from the initial state of tG, which is believed to be a mixed state of open and the dimer form of tG, and that the overall dimer fraction increases (manuscript in preparation). This transition was undetectable with static SAXS, and the Kenics mixer was the ideal tool to capture the monomer to dimer transition of tG, especially since our static SAXS measurements show the formation of aggregates on timescales of 5-30 minutes.

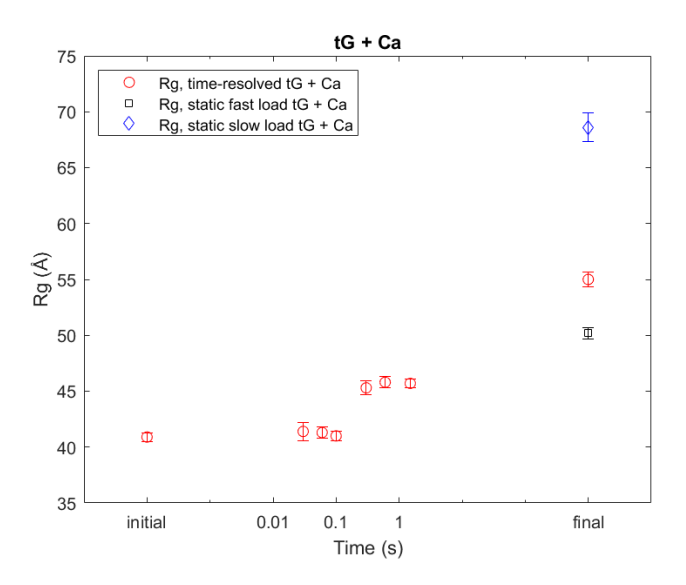


**Figure 6** The  $R_g$  of tG as calcium binds and triggers a conformational change. Three different endpoints are also shown to demonstrate the aggregation of tG at longer timepoints that are typical for conventional equilibrium SAXS measurements. Fast load corresponds to a 5 minute incubation and slow load corresponds to a 30 minute incubation.

## 3.2.3. Binding of Trypsin and Aprotinin

The above examples illustrate the mixing of large and small reacting species. However, the most unique feature of the Kenics insert is its ability to rapidly combine and follow reactions between two large species. Reactions between two macromolecules can also be studied with a stopped flow mixer, but the Kenics approach reduces sample consumption. As proof of principle, we examined binding of a model system comprised of the proteins aprotinin and trypsin. We flowed trypsin through one side of the Kenics (cone opening device, Reaction Class 1) and aprotinin through the other so that we could observe the reaction's time evolution. We collected the two initial states (trypsin alone and aprotinin alone), a steady state (trypsin and aprotinin incubated together), and seven intermediate timepoints (10 ms, 32 ms, 100 ms, 400 ms, 631 ms, 1000 ms, and 2000 ms; Figure 7). Again, using the R<sub>g</sub> as the reaction metric, we measure a steady increase with time, indicating binding. At 2000 ms, the complex appears to be already fully formed. Because aprotinin is a small protein, with molecular weight of 7 kDa, its binding to trypsin (24 kDa) does not yield a large change in the overall R<sub>e</sub>. However, it is too large (diffusion too slow) to mix via a flow focusing diffusive mixer. We also used this model system to assess the reproducibility of the Kenics mixer. Importantly, we showed that the same timepoint could be measured with different flow conditions, by adjusting the measurement position distance from the tip, to yield nearly identical scattering profiles (Figure S5).

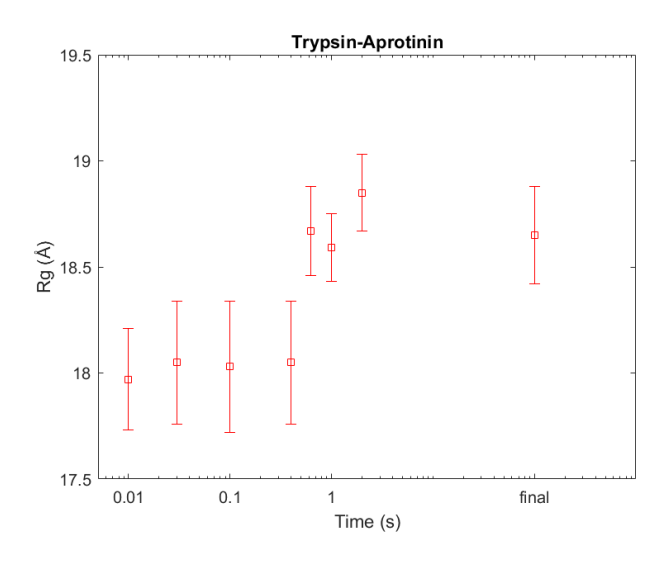


**Figure 7** Changes in the R<sub>g</sub> as trypsin and aprotinin bind, even these small changes can be captured.

## 3.2.4. Evolution of GAC rRNA + L11 Protein Complex

This last example considers mixing of two comparably sized macromolecules, an rRNA fragment with a molecular weight of 18.7 kDa and a protein domain with a molecular weight of 15.6 kDa. Protein-nucleic acid complexes, especially RNA-protein complexes, are biologically important, yet poorly understood. The chaotic advection mixer provides the opportunity to study the structural changes that immediately follow (or precede) binding of two moderately sized macromolecules. The small GAC rRNA discussed above is part of the 23S bacterial ribosome. In the ribosome, its biological partner is the protein L11. Crystal structures show that the protein stabilizes the tertiary fold of the functional RNA (Blyn et al., 2000). In previous work (Welty et al., 2020), we stipulated that the C-terminal domain of the L11 protein binds RNA during its Mg<sup>2+</sup>-dependent folding trajectory. Here, we examine binding of the RNA to the full length L11 protein (Jonker et al., 2007). To study this reaction, we used the Kenics (cone opening device, Reaction Class 1) to mix unstructured GAC rRNA in KCl with L11 protein in MgCl<sub>2</sub>. We collected two initial states (GAC rRNA alone, no Mg<sup>2+</sup>, and L11 alone, with Mg<sup>2+</sup>), one final state (GAC rRNA, L11, and Mg<sup>2+</sup> incubated together for several minutes), and ten intermediate timepoints (30 ms, 50 ms, 63 ms, 100 ms, 200 ms, 316 ms, 631 ms, 1000 ms, and 2000 ms). As we mix GAC rRNA with L11 in MgCl<sub>2</sub>, the R<sub>g</sub> steadily increases with time, supporting the model that L11 stabilizes the folded RNA as they bind.

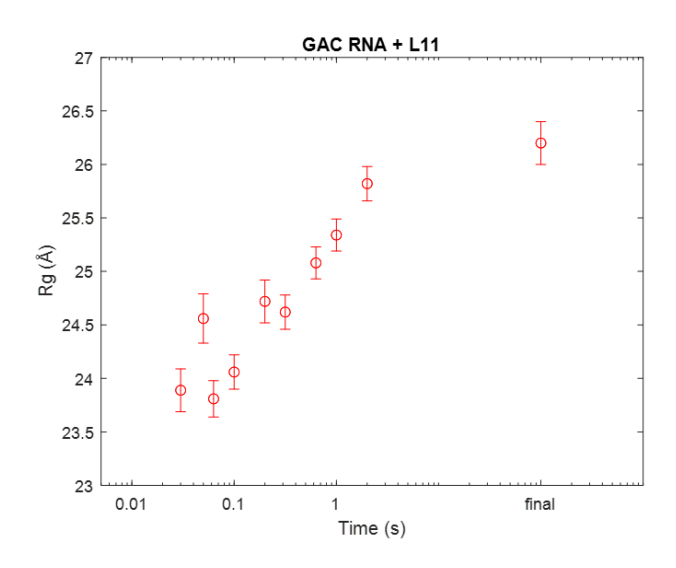


**Figure 8** The R<sub>g</sub> change of the association of GAC rRNA with its L11 protein partner.

#### 4. Discussion

Here we demonstrated that a chaotic advection mixer, with a Kenics design, is extremely versatile and enables triggering and monitoring of reactions involving widely sized pairs of reactants. Its use was demonstrated in four different experiments, following the mixing of: RNA with ions (GAC rRNA with Mg<sup>2+</sup>), protein with ions (tG with Ca<sup>2+</sup>), protein with protein (trypsin with aprotinin), and RNA with protein (GAC rRNA with L11 protein). In each case, we observed dynamics on time scales relevant for conformation dynamics in many systems, ranging from 10 ms through 2000 ms. The high efficiency mixing of the Kenics design, based on a baker's transformation, is the key to its flexibility when applied to this broad ranging group of reactions. The resulting fast mixing also leads to lower uncertainty in each measurement, illustrated by the smaller size in the error bars for the Rg measurements carried out with a Kenics mixer and a flow focusing counterpart (Figure 5B). This lower uncertainty is a particular advantage when measuring at the fastest timepoints, and especially for processes that are complete on this time scale. The decreased spread in overall age of the reaction means that distinct intermediates will be easier to resolve.

We also described an efficient and sample-minimizing loop-loading system that requires 75  $\mu$ L of sample and 150  $\mu$ L of buffer for each timepoint. This volume is on par with what is required for a single SAXS measurement at most synchrotrons. It represents a significant reduction from the ~hundreds of microliters per timepoint required for both turbulent and stopped flow mixers. Additionally, the continuous flow nature of Kenics mixer still allows for radiation damage limits to be avoided, like the turbulent mixer, but at much lower flowrates, due in part to the sheath flow surrounding the sample stream. With this moderate sample consumption, an entire time series with 7 timepoints can be collected with only ~500  $\mu$ L of sample and in approximately 3 hours (including cleaning times and reloading), allowing for collection of multiple time series with different molecules

during a single, days-long beamtime. This efficiency is particularly advantageous when performing mixing experiments with the same biomolecule, but different ligands, as a single batch of the biomolecule could be used. Thus, experiments probing the interaction of a single protein with different partner molecules, can be performed under as close to identical conditions as possible to help answer biological questions.

Furthermore, there is a large demand for structural information of ligand binding events to help drive drug design and even the moderate resolution range of SAXS is sufficient to gain some mechanistic understanding of these events (Aplin *et al.*, 2022). Both our tG + Ca<sup>2+</sup> and trypsin + aprotinin experiments demonstrate that protein dynamics and structural information can be captured with our device. Additionally, our myoglobin and azide time-resolved absorbance experiments show that accurate k values can be extracted from data taken with our Kenics mixer. Therefore, this mixer may contribute to time-resolved structural studies of drug-target interactions through both structural and kinetic measurements. Because accurate determinations of kinetic rate parameters require measurements at known, fixed concentrations of small compounds, the Kenics style mixer is very well suited for these measurements. There is the potential to use the structural mechanistic information gained by TR-SAXS and kinetics experiments with the Kenics to alter ligand designs to go from micromolar to nanomolar binding affinities.

Finally, because of its flexible design, the mixing insert can be combined with additional structural or spectroscopic probes that provide information complementary to SAXS. These mixers can be readily coupled with simple-to-design outlet configurations that enable measurements by X-ray spectroscopies, crystallography, or cryo-EM techniques. In addition, due to the ease of fabrication by 3D printing, mixing can be optimized for systems containing larger particles such as microcrystals. The versatile mixer system described here can be coupled with a wide variety of mix-and-inject systems. With the sample efficient loading described herein, a broad range of biologically important reactions can be probed on the time scales relevant to conformational dynamics.

#### 5. Conclusion

We report the design, operation, and use of a 3D-printed Kenics-style chaotic advection mixer to probe reactions involving classes of biological macromolecules with each other, or with a wide variety of small molecules. The information revealed will improve our understanding of important biophysical and medical processes, ranging from probing the underlying physics of macromolecular self-assembly, to improving structure-based drug design.

**Acknowledgements** We thank Richard Gillilan for experimental assistance at CHESS. We thank Juraj Knoška for 3D printing assistance.

**Funding Information** This work is/was supported by grants from the National Institutes of Health (NIH) grants R35-GM122514, T32-GM008267, R35GM122175, CA201402, CA223534, and the National Science Foundation (NSF) under award DBI-1930046 and STC award #1231306. SAXS data were acquired at the Sector 7A1 beamline at CHESS, supported by NSF & National Institutes of Health/National Institute of General Medical Sciences (NIH/NIGMS) via NSF award (DMR-0936384 to CHESS). SAXS data were also acquired on a Xenocs BioXolver acquired through NIH grant S10OD028617.

**Current Affiliations** AMK and GDC are now at Kimball Physics Inc., Wilton, NH, USA; SAP is now at Analytical Research and Development, Merck & Co., Inc., West Point, PA, USA; JSE is now at Xenocs Inc., Holyoke, MA, USA.

#### References

Aplin, C., Milano, S. K., Zielinski, K. A., Pollack, L. & Cerione, R. A. (2022). *J. Phys. Chem. B* acs.jpcb.2c04344.

Benkovic, S. J. (2003). Science 301, 1196–1202.

Bertsch, A., Heimgartner, S., Cousseau, P. & Renaud, P. (2001). Lab Chip 1, 56.

Blyn, L. B., Risen, L. M., Griffey, R. H. & Draper, D. E. (2000). *Nucleic Acids Research* 28, 1778–1784.

Calvey, G. D., Katz, A. M., Schaffer, C. B. & Pollack, L. (2016). Struct. Dyn. 3, 054301.

Calvey, G. D., Katz, A. M., Zielinski, K. A., Dzikovski, B. & Pollack, L. (2020). *Anal. Chem.* 92, 13864–13870.

Cho, H. S., Schotte, F., Stadnytskyi, V. & Anfinrud, P. (2021). *Current Opinion in Structural Biology* **70**, 99–107.

Datta, S., Antonyak, M. A. & Cerione, R. A. (2006). *Biochemistry* 45, 13163–13174.

Datta, S., Antonyak, M. A. & Cerione, R. A. (2007). Biochemistry 46, 14819–14829.

Draper, D. E. (2004). RNA 10, 335-343.

Frank, J. (2017). Journal of Structural Biology 200, 303–306.

Galaktionov, O. S., Anderson, P. D., Peters, G. W. M. & Meijer, H. E. H. (2003). *International Polymer Processing* **18**, 138–150.

Graceffa, R., Nobrega, R. P., Barrea, R. A., Kathuria, S. V., Chakravarthy, S., Bilsel, O. & Irving, T. C. (2013). *J Synchrotron Rad* **20**, 820–825.

Grilley, D., Misra, V., Caliskan, G. & Draper, D. E. (2007). *Biochemistry* 46, 10266–10278.

Hobbs, D. M. & Muzzio, F. J. (1997). Chemical Engineering Journal 67, 153–166.

- Jonker, H. R. A., Ilin, S., Grimm, S. K., Wöhnert, J. & Schwalbe, H. (2007). *Nucleic Acids Research* 35, 441–454.
- Katt, W. P., Antonyak, M. A. & Cerione, R. A. (2018). Drug Discovery Today 23, 575–591.
- Katt, W. P., Aplin, C. & Cerione, R. A. (2022). Onco Targets Ther 15, 277–290.
- Khaykelson, D. & Raviv, U. (2020). *Biophys Rev* 12, 41–48.
- Kikhney, A. G. & Svergun, D. I. (2015). FEBS Letters 589, 2570–2577.
- Kirby, N., Cowieson, N., Hawley, A. M., Mudie, S. T., McGillivray, D. J., Kusel, M., Samardzic-Boban, V. & Ryan, T. M. (2016). *Acta Crystallogr D Struct Biol* **72**, 1254–1266.
- Knoška, J., Adriano, L., Awel, S., Beyerlein, K. R., Yefanov, O., Oberthuer, D., Peña Murillo, G. E., Roth, N., Sarrou, I., Villanueva-Perez, P., Wiedorn, M. O., Wilde, F., Bajt, S., Chapman, H. N. & Heymann, M. (2020). *Nat Commun* 11, 657.
- Kučerka, N., Nagle, J. F., Sachs, J. N., Feller, S. E., Pencer, J., Jackson, A. & Katsaras, J. (2008). *Biophysical Journal* **95**, 2356–2367.
- Lamb, J., Kwok, L., Qiu, X., Andresen, K., Park, H. Y. & Pollack, L. (2008). *J Appl Crystallogr* **41**, 1046–1052.
- Li, Y., Beck, R., Huang, T., Choi, M. C. & Divinagracia, M. (2008). *J Appl Crystallogr* **41**, 1134–1139.
- Liu, S., Cerione, R. A. & Clardy, J. (2002). Proc. Natl. Acad. Sci. U.S.A. 99, 2743–2747.
- Lu, Z., Shaikh, T. R., Barnard, D., Meng, X., Mohamed, H., Yassin, A., Mannella, C. A., Agrawal, R. K., Lu, T.-M. & Wagenknecht, T. (2009). *Journal of Structural Biology* **168**, 388–395.
- Mann, A. P., Verma, A., Sethi, G., Manavathi, B., Wang, H., Fok, J. Y., Kunnumakkara, A. B., Kumar, R., Aggarwal, B. B. & Mehta, K. (2006). *Cancer Res* **66**, 8788–8795.
- Marcoline, A. T. & Elgren, T. E. (1998). Journal of Chemical Education 75, 1622–1623.
- Martin, E. W., Harmon, T. S., Hopkins, J. B., Chakravarthy, S., Incicco, J. J., Schuck, P., Soranno, A. & Mittag, T. (2021). *Nat Commun* 12, 4513.
- Maruo, S., Nakamura, O. & Kawata, S. (1997). Optics Letters 22, 132–134.
- Moffat, K. (1998). Acta Crystallographica Section A 54, 833–841.
- Monteiro, D. C. F., Amoah, E., Rogers, C. & Pearson, A. R. (2021). *Acta Crystallogr D Struct Biol* 77, 1218–1232.
- Nami, F., Gast, P. & Groenen, E. J. J. (2016). Appl Magn Reson 47, 643–653.
- Nielsen, S. S., Toft, K. N., Snakenborg, D., Jeppesen, M. G., Jacobsen, J. K., Vestergaard, B., Kutter, J. P. & Arleth, L. (2009). *J Appl Crystallogr* **42**, 959–964.
- Niesler, F. & Hermatschweiler, M. (2014). Laser Technik Journal 11, 16–18.
- van Nuland, N. A. J., Forge, V., Balbach, J. & Dobson, C. M. (1998). Acc. Chem. Res. 31, 773–780.

- Olmos, J. L., Pandey, S., Martin-Garcia, J. M., Calvey, G., Katz, A., Knoska, J., Kupitz, C., Hunter, M. S., Liang, M., Oberthuer, D., Yefanov, O., Wiedorn, M., Heyman, M., Holl, M., Pande, K., Barty, A., Miller, M. D., Stern, S., Roy-Chowdhury, S., Coe, J., Nagaratnam, N., Zook, J., Verburgt, J., Norwood, T., Poudyal, I., Xu, D., Koglin, J., Seaberg, M. H., Zhao, Y., Bajt, S., Grant, T., Mariani, V., Nelson, G., Subramanian, G., Bae, E., Fromme, R., Fung, R., Schwander, P., Frank, M., White, T. A., Weierstall, U., Zatsepin, N., Spence, J., Fromme, P., Chapman, H. N., Pollack, L., Tremblay, L., Ourmazd, A., Phillips, G. N. & Schmidt, M. (2018). *BMC Biology* 16, 59.
- Pandey, S., Calvey, G., Katz, A. M., Malla, T. N., Koua, F. H. M., Martin-Garcia, J. M., Poudyal, I., Yang, J.-H., Vakili, M., Yefanov, O., Zielinski, K. A., Bajt, S., Awel, S., Doerner, K., Frank, M., Gelisio, L., Jernigan, R., Kirkwood, H., Kloos, M., Koliyadu, J., Mariani, V., Miller, M. D., Mills, G., Nelson, G., Olmos, J. L., Sadri, A., Sato, T., Tolstikova, A., Xu, W., Ourmazd, A., Spence, J. C. H., Schwander, P., Barty, A., Chapman, H. N., Fromme, P., Mancuso, A. P., Phillips, G. N., Bean, R., Pollack, L. & Schmidt, M. (2021). *IUCrJ* 8, https://doi.org/10.1107/S2052252521008125.
- Panine, P., Finet, S., Weiss, T. M. & Narayanan, T. (2006). *Advances in Colloid and Interface Science* **127**, 9–18.
- Pinkas, D. M., Strop, P., Brunger, A. T. & Khosla, C. (2007). PLoS Biol 5, e327.
- Plaxco, K. W. & Dobson, C. M. (1996). Current Opinion in Structural Biology 6, 630–636.
- Plumridge, A., Katz, A. M., Calvey, G. D., Elber, R., Kirmizialtin, S. & Pollack, L. (2018). *Nucleic Acids Research* **46**, 7354–7365.
- Pollack, L. & Doniach, S. (2009). Vol. 469, Methods in Enzymology. pp. 253–268. Elsevier.
- Pollack, L., Tate, M. W., Darnton, N. C., Knight, J. B., Gruner, S. M., Eaton, W. A. & Austin, R. H. (1999). *Proceedings of the National Academy of Sciences* **96**, 10115–10117.
- Pollack, L., Tate, M. W., Finnefrock, A. C., Kalidas, C., Trotter, S., Darnton, N. C., Lurio, L., Austin, R. H., Batt, C. A., Gruner, S. M. & Mochrie, S. G. J. (2001). *Phys. Rev. Lett.* **86**, 4962–4965.
- Saatdjian, E., Rodrigo, A. J. S. & Mota, J. P. B. (2012). Chemical Engineering Journal 187, 289–298.
- Sobiesierski, A., Thomas, R., Buckle, P., Barrow, D. & Smowton, P. M. (2015). *Surface and Interface Analysis* **47**, 1174–1179.
- Squires, T. M. & Quake, S. R. (2005). Rev. Mod. Phys. 77, 977–1026.
- Svergun, D. I. & Koch, M. H. J. (2003). Rep. Prog. Phys. 66, 1735–1782.
- Szalai, E. S. & Muzzio, F. J. (2003). AIChE Journal 49, 2687–2699.
- Thompson, M. C., Barad, B. A., Wolff, A. M., Sun Cho, H., Schotte, F., Schwarz, D. M. C., Anfinrud, P. & Fraser, J. S. (2019). *Nat. Chem.* **11**, 1058–1066.
- Triantafillidou, D., Simitsopoulou, M., Franceschi, F. & Choli-Papadopoulou, T. (1999). *Journal of Protein Chemistry* **18**, 215–223.
- Wang, Z., Stangegaard, M., Dufva, M., Kutter, J., Wolff, A. & Wang, Z. (2005). *Proc. UTAS 2005* **2**, 745–747.

- Welty, R., Pabit, S. A., Katz, A. M., Calvey, G. D., Pollack, L. & Hall, K. B. (2018). RNA 24, 1828–1838.
- Welty, R., Rau, M., Pabit, S., Dunstan, M. S., Conn, G. L., Pollack, L. & Hall, K. B. (2020). *Journal of Molecular Biology* **432**, 991–1007.
- Wiggins, S. & Ottino, J. M. (2004). *Philosophical Transactions of the Royal Society of London. Series A: Mathematical, Physical and Engineering Sciences* **362**, 937–970.
- Young, M. E., Carroad, P. A. & Bell, R. L. (1980). Biotechnology and Bioengineering 22, 947–955.